This is a repository copy of *The Uptake of HO₂ on Meteoric Smoke Analogues*.

Article:

1   # The Uptake of HO$_2$ on Meteoric Smoke Analogues

2

3   Alexander D. James[1], Daniel R. Moon[1], Wuhu Feng[1,2], Pascale S. J. Lakey[1,3], Victoria L.

4   Frankland[1], Dwayne E. Heard[1,2] & John M. C. Plane[1]*

5

6   1. School of Chemistry, University of Leeds, Leeds, LS2 9JT, UK

7   2. National Centre for Atmospheric Science, University of Leeds, Leeds, UK

8   3. Max Planck Institute for Chemistry, Hahn-Meitner-Weg 1,

9   55128 Mainz

10

11   * Corresponding author: j.m.c.plane@leeds.ac.uk, +44 113 3438044

12

14

1

15 **Abstract**

16 The kinetics of heterogeneous HO_2 uptake onto Meteoric Smoke Particles (MSPs) has been

17 studied in the laboratory using analogues of MSP aerosol entrained into a flow tube. The

18 uptake coefficient, γ, was determined on synthetic amorphous olivine ($MgFeSiO_4$) to be

19 $(6.9 \pm 1.2) \times 10^{-2}$ at a relative humidity (RH) of 10%. On forsterite (Mg_2SiO_4),

20 $\gamma = (4.3 \pm 0.4) \times 10^{-3}$ at RH = 11.6%, and $(7.3 \pm 0.4) \times 10^{-2}$ at RH = 9.9% on fayalite (Fe_2SiO_4).

21 These results indicate that Fe plays a more important mechanistic role than Mg in the

22 removal of HO_2 from the gas phase. Electronic structure calculations show that Fe atoms

23 exposed at the particle surface provide a catalytic site where HO_2 is converted to H_2O_2 *via*

24 an Eley-Rideal mechanism, but this does not occur on exposed surface Mg atoms. The

25 impact of this heterogeneous process in the middle atmosphere was then investigated using

26 a whole atmosphere chemistry-climate model which incorporates a microphysical treatment

27 of MSPs. Using a global MSP production rate from meteoric ablation of 44 tons per day,

28 heterogeneous uptake (with $\gamma = 0.2$) on MSPs significantly alters the HO_x budget in the

29 night-time polar vortex. This impact is highly latitude dependent and thus could not be

30 confirmed using currently available satellite measurements of HO_2, which are largely

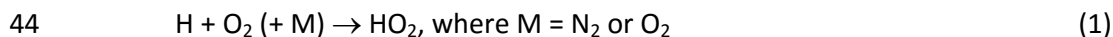31 unavailable at latitudes greater than 70°.

32

33

34

35

36

37

38

39

Introduction

A significant discrepancy exists between observations and model predictions of HO_2 concentrations in the middle atmosphere, known as the 'HO$_x$ dilemma' [*Millán et al.*, 2015]. *Siskind et al.* [2013] showed that increasing the rate coefficient for the reaction

$$H + O_2 (+ M) \rightarrow HO_2, \text{ where M = N}_2 \text{ or O}_2 \tag{1}$$

by a factor of ~1.5 improved agreement to the observed OH profile, but did not present a detailed comparison for HO_2. *Pickett et al.* [2008] found that for northern hemisphere summer, rate constants within the stated error of the JPL 2006 recommendation could explain the observed HO_2 but did not discuss other seasons or latitudes. In general, a kinetic description which underpredicts HO_2 density in the upper mesosphere results in over-prediction in the lower mesosphere / stratosphere and *vice versa* [*Millán et al.*, 2015].

The modelling studies discussed above consider only gas-phase chemistry. In terms of heterogeneous chemistry, noctilucent clouds occur in the polar summer mesosphere above 80 km, causing perturbations to atomic O and HO$_x$ around the ice clouds [*Murray and Plane*, 2005]. However, in the middle mesosphere below 80 km the only known source of potentially reactive surfaces are Meteoric Smoke Particles (MSPs). These particles form by recondensation of the metallic vapours which are released by meteoric ablation [*Hunten et al.*, 1980; *Plane et al.*, 2015] and are likely composed of Fe-Mg-silicates [*Saunders and Plane*, 2006]. Recent studies have shown that uptake on MSPs may significantly affect the atmospheric abundance of species such as HNO_3 and H_2SO_4 in the stratosphere/lower mesosphere [*Frankland et al.*, 2015; *Saunders et al.*, 2012]. The heterogeneous recombination of O and H_2 on MSPs has also been suggested as a source of H_2O in the lower mesosphere [*Summers and Siskind*, 1999].

A study of the heterogeneous chemistry of HO_2 on MSPs is therefore timely. Here we report an experimental measurement of the uptake coefficient, γ, for HO_2 on a variety of MSP analogues, which were prepared using a sol-gel process that we have described previously [*Frankland et al.*, 2015]. The uptake rate was measured by entraining these particles in a laminar gas flow, and detecting HO_2 by conversion to OH and the Fluorescence Assay by Gas Expansion (FAGE) technique [*Matthews et al.*, 2014].

3

69   The Fluorescence Assay by Gas Expansion (FAGE) technique is used to detect HO_2 radicals

70   with very high sensitivity, building from extensive experience in measuring these radicals in

71   the field [*Stone et al.*, 2012]. Briefly, gas is sampled at the end of the aerosol flow-tube by a

72   small circular pinhole (diameter 0.7 mm), at which point the gas expands supersonically into

73   a low pressure fluorescence cell, and the gas jet is crossed by a laser beam ~ 120 mm from

74   the pinhole. The background pressure in the cell is held at ~ 1 Torr, with the fast flow of gas

75   maintained by a rotary pump/roots blower combination, and close to the pinhole nitric

76   oxide (NO, 99.5.%, BOC) is added to convert HO_2 to OH radicals, which are detected by laser-

77   induced fluorescence exciting at a wavelength of ~308 nm (from a high pulse-repetition-

78   frequency Nd: YAG pumped dye laser) using the $Q_1(2)$ rotational transition of the

79    $A^2\Sigma$ (v′=0) - $X^2\Pi_{3/2}$ (v″=0) vibronic band of OH. On-resonant fluorescence is collected *via* the

80   same band, using a series of fast lenses and an interference filter centred at 308 nm, and in

81   order to discriminate against the more intense laser scattered light, the fluorescence, whose

82   lifetime is extended at the low pressure, is detected *via* delayed photon counting. The

83   detector (Perkin Elmer 993P) is gated off during the laser-pulse to avoid saturation from the

84   scattered light. The sensitivity of the HO_2 detection is calibrated using a known

85   concentration of HO_2 generated from the photolysis of water vapour at 185 nm in presence

86   of zero air (Whalley et al., 2011, George et al., 2013, Matthews et al., 2014), and is ~ 10^6

87   molecule cm^{-3}.

88   A version of the Whole Atmosphere Community Climate Model (WACCM) coupled with the

89   Community Aerosol and Radiation Model for Atmospheres (CARMA) which includes a

90   treatment of MSP microphysics [*Bardeen et al.*, 2008], was then used in order to determine

91   if MSPs can have an impact on the HO_x budget. Because of uncertainties in the uptake

92   coefficients this study does not attempt to quantify any such impact. Rather the modelling

93   presented here is intended to give the reader an idea of when and where such an impact

94   might occur.

95   **Experimental Method**

96   MSP analogues in the form of amorphous compounds with olivine compositions

97    $Mg_xFe_{2-x}SiO_4$ (where $0 \leq x \leq 2$) were produced by mixing stoichiometric quantities (relative

98   to 0.1 molar product) of aqueous solutions of magnesium chloride (Aldrich), ferrous (II)

4

99   ammonium sulfate (Sigma-Aldrich) and sodium orthosilicate (Alfa Aesar) at room

100   temperature for 7 days [*Frankland et al.*, 2015]. Metal-salt by-products were removed from

101   products by repeated dialysis using a soxhlet apparatus with the particles held in water-

102   permeable tubing (Snakeskin 7000 MWCO). This method was used to produce materials

103   with x = 0, 1 and 2. Although the products are amorphous, they will hereafter be referred to

104   respectively as fayalite, olivine and forsterite for simplicity.

105   The experimental procedure for measuring the HO_2 uptake coefficients has been described

106   in detail elsewhere [*George et al.*, 2013; *Matthews et al.*, 2014]. An experimental diagram is

107   shown in Figure 1.

108   Details of the gas flow control system are given in *Matthews et al.* [2014] which described

109   uptake experiments onto Arizona Test Dust aerosols. The carrier gas used for these

110   experiments was compressed nitrogen which first passed through a gas purification system

111   consisting of particle filters, a dryer and a carbon filter. The HO_2 flow, the humidified flow

112   and the NO flow were controlled using five mass flow controllers (Brooks, model 5850S and

113   MKS, model 1179A). The required Relative Humidity (RH) was obtained by mixing together

114   and altering the ratio of a dry flow and a flow which had been passed through a water

115   bubbler (Milli-Q, 18 MΩ cm). This humidified flow, which was mixed with the aerosol flow in

116   the conditioning flow tube, was ∼ 3 litres per minute (lpm) throughout each individual

117   experiment. The aerosol flow was monitored and maintained at 1.0 ± 0.1 lpm and the HO_2

118   flow from the injector (which is moved to provide varied contact times in random order)

119   was measured as 1.3 ± 0.05 lpm. The total flow passing through the flow tube (with 5.9 cm

120   diameter), including the aerosol, dilution and HO_2 flows, was ∼5.3 ± 1 lpm (variations are

121   due to the mixing of dry and humid flows). The FAGE instrument sampled ∼ 4.2 lpm and the

122   Condensation Particle Counter (CPC, TSI 3775) sampled 0.3 lpm with the remainder of the

123   flow (∼0.8 lpm) exiting *via* an exhaust line. The pressure and temperature in the aerosol

124   flow-tube were maintained at atmospheric pressure and room temperature (∼20-22°C).

125   MSP aerosols were entrained in the carrier gas using either a magnetic stirrer (shown in

126   Figure 1) or acoustic dust disperser and passed through an impactor (TSI 1034900, nozzle

127   diameter 0.71 mm, D_{50} = 1286 nm), which was used to stabilise the flow rate from the dust

128   disperser. The concentration of aerosols entering the flow tube was controlled using a High

129   Efficiency Particulate Air (HEPA) filter and a bypass. The proportion of the flow passing

      5

130   through the bypass compared to the filter was controlled using a needle valve (not shown in

131   Figure 1). The aerosol number concentration was monitored using a CPC. Measurements

132   were also made either immediately before or after each uptake experiment, under the same

133   experimental conditions, using a Scanning Mobility Particle Sizer (SMPS, TSI, 3080) in order

134   to measure the entire log normal size distribution. Checks determined that the average

135   radius did not change over time or when sampling from before or after the flow tube. The

136   size distribution was independent of whether HO_2 was flowing from the injector or not.

137   HO_2 was formed by passing water vapour in front of a mercury pen-lamp to form OH and H;

138   HO_2 is then produced when the latter reacts with trace O_2 impurity in the N_2 carrier gas. This

139   produces an initial HO_2 concentration in the second flow tube of 1.6×10^9 molecules cm^{-3}.

140   Variability in the HO_2 signal due to lamp output and supplied humidity (controlled by flow

141   controllers) is very small. The absolute concentration downstream is known following

142   calibration of the sensitivity of the fluorescence cell [*George et al.*, 2013]. The injector was

143   used to vary the contact time of the HO_2 with the aerosol to determine the uptake kinetics.

144   Experiments were performed on all 3 MSP analogue materials.

145   **Results and Discussion**

146   ***Measured size distributions***

147   A typical set of 10 measured size distributions is shown for fayalite at 9.9 % RH in Figure 2.

148   The mean, which is used to calculate the experimental surface area, is shown in black. This

149   shows that, while there is some variability in the output of the aerosoliser, a log normal

150   distribution is measured and can be well characterised (in this case the distribution had a

151   mean of 368 nm and a standard deviation of 0.680). This gives a measurement of the mean

152   surface area of each MSP (4.25×10^{-9} cm^2 in this example). CPC measurements of the

153   number concentration are used during experiments to calculate the total available surface

154   area.

155   The spherical assumption used here for the particles neglects any surface roughness and

156   may lead to an underestimation of the surface area available for HO_2 to interact with. This

157   would result in an overestimation of the uptake coefficient [*Frankland et al.*, 2015].

158   *Measurements of the uptake coefficient,*

159   A clear uptake of HO_2 to the MSP analogues was observed in all experiments. Figure 3 (a)

160   illustrates the relationship between the fayalite aerosol number concentration and HO_2

161   signal in a typical experiment where the RH was 9.9 % and residence time of 20.6 s. Raw HO_2

162   signal is shown. Before further analysis the data were corrected for the output power of the

163   laser. The reference cell signal would also enable any drifts in laser power or wavelength to

164   be monitored, and is used to centre the laser wavelength on the OH transition. If the

165   reference cell changes significantly (but not the laser power) then the data are not used so

166   the laser power is considered a good reference for normalisation. Since uptake is a first-

167   order process, the HO_2 concentration $[HO_2]_t$ is then related kinetically to the available

168   aerosol surface and the initial concentration $[HO_2]_0$ by

169     $$-\ln \frac{[HO_2]_t}{[HO_2]_0} = 0.25\gamma_{obs} w A_d N_d t + k_W t \qquad \text{(E1)}$$

170   where γ_{obs} is the observed uptake coefficient, w the molecular mean speed (cm s^{-1}), N_d the

171   number density of aerosol (cm^{-3}), A_d the surface area of the mean aerosol particle (cm^2), t

172   the contact time (s) during which HO_2 can adsorb onto the particles, and k_w the rate

173   coefficient for loss (s^{-1}) of HO_2 on the flowtube walls and by self-recombination in the gas-

174   phase to form H_2O_2. This is determined by measuring uptake without the aerosol flow for

175   several injector positions at the beginning and end of each experiment (under the same RH

176   conditions). It should be noted that at HO_2 concentration of ~10^9 molecule cm^{-3} the loss via

177   the gas phase reaction is very small (e-folding lifetime >100 s). At the pressure of 1 bar used

178   in these experiments, diffusional transport of HO_2 to the particle surface is not in the free

179   molecular regime, so γ_{obs} was then corrected for slip flow [*Matthews et al.*, 2014]:

180     $$\gamma = \frac{\gamma_{obs}}{1-\gamma_{obs}\lambda(r_s)} \qquad \text{(E2)}$$

181   where $\lambda(r_s)$, the mean free path for a particle of radius r_s, is given by

182     $$\lambda(r_s) = \frac{0.75+0.28Kn}{Kn(1+Kn)} \qquad \text{(E3)}$$

183   where Kn, the Knudsen number, is given by

184     $$Kn = \frac{3D_g}{wr_s} \qquad \text{(E4)}$$

7

185 and D_g is the diffusion constant for HO$_2$, taken to be 0.25 cm^2 s^{-1} at 1 bar [*Mozurkewich et*

186 *al.*, 1987]. This results in a range of *Kn* from 1.26 for the smallest to ~0.3 for the largest

187 particles. The contact time *t* was determined for the experimental flow conditions (Reynolds

188 number = 136) by applying the Brown correction to the plug flow time determined from the

189 mass flow rates and pressure [*Brown*, 1978]. Figure 3 (b) shows that ln[HO$_2$]$_t$ was linearly

190 anti-correlated with N_d, in accord with equation (E1), so the slope is equal to $0.25\gamma_{obs}wA_dt$

191 ((6.3 ± 1.4) × 10^{-6} in this case). The slope was then measured over a range of contact times

192 and found to vary linearly as shown in Figure 4 (a) (for fayalite at RH of 9.9 %, R^2=0.945). The

193 mean aerosol surface area determined from a log-normal fit to the SMPS data and the

194 gradient of the line in Figure 4 (a) was used to determine γ.

195 *Matthews et al.* [2014] suggested that a positive intercept on a plot such as Figure 4 (a) can

196 be indicative of some experiments occurring at contact times too short for HO$_2$ to reach

197 equilibrium with the surface. By plotting a line from the origin to each point in Figure 4 (a),

198 the change in uptake coefficient over time can be quantified. This is shown in Figure 4 (b).

199 Some surface sites in these experiments appear to be deactivated as the HO$_2$ comes to

200 equilibrium with the MSP analogues. The probability of uptake is less at equilibrium (when

201 some sites are occupied) than for surfaces which have had contact times too short to reach

202 equilibrium. Note that the uptake coefficient at long times approaches that calculated from

203 the fit to the whole data set. These values should be taken as the true measurement of

204 uptake, since they correspond to HO$_2$ in equilibrium with the surface. Any change in the

205 system as a result of the experimental process, *e.g.* deposition of analogue particles in the

206 flow tube, could also lead to changes in the intercept of plots such as Figure 4 (a) but since

207 the measurements at different contact times are performed in random order this could not

208 explain the observed larger uptake coefficients for points at shorter contact times.

209 Surface coverage of HO$_2$ can be further investigated by estimating the mean distance

210 between HO$_2$ molecules on the surface at the longest contact times, assuming that all HO$_2$

211 which are taken up remain on the surface. This is done by integrating the loss of HO$_2$ with

212 respect to time to determine the total adsorbed on dust of known surface area, and

213 assuming the HO$_2$ molecules are dispersed isentropically over the surface. The smallest

214 distance estimated here was 10 Å, implying that a significant proportion of the surface sites

215 might have become saturated. However, the linearity of plots such as those shown in

216   Figures 4 (a) implies that there was no deviation from constant first-order uptake kinetics.

217   This suggests that HO_2 is converted to other products and many of the available surface

218   sites are re-activated. This is discussed further in the light of electronic structure calculations

219   below.

220   *Matthews et al.* [2014] also found that the uptake coefficient decreased by a factor of two

221   with a four fold increase in the initial concentration of HO_2. Since the mechanism in both

222   cases is likely driven by Fe active sites [*Broadley et al.*, 2012], we would expect a similar

223   trend here. Equivalent experiments, which are technically challenging and cannot cover a

224   large range of $[HO_2]_0$, were therefore not performed in this study. γ values measured in this

225   study are summarised in Table 1. The larger γ values measured on olivine and fayalite

226   suggest that HO_2 is taken up more readily by Fe compared with Mg active sites on the MSP

227   analogue surface.

228   A number of previous studies have concluded that HO_2 uptake could be driven by the

229   presence of Transition Metal Ions (TMIs) at the particle surface or in the bulk of a liquid

230   particle eg. [*Lakey et al.*, 2015]. *Mao et al.* [2013] demonstrated that where Fe and Cu ions

231   are both present in a liquid droplet redox chemistry can lead to the production of H_2O

232   rather than H_2O_2. These mechanisms are not likely to be important here, however, since for

233   TMIs to be available in a liquid droplet would require both RH approaching 100% and a

234   soluble solid. Since by-products of the synthesis process are removed from the MSP

235   analogues by repeated dialysis in near boiling point water, it is unlikely that any soluble

236   material remains.

237   ***Electronic structure calculations***

238   In order to investigate the mechanism for HO_2 uptake on the MSP analogue surfaces, we

239   employed electronic structure calculations using the Gaussian 09 suite of programs [*Frisch*

240   *et al.*, 2009]. The hybrid density functional/Hartree-Fock B3LYP method was employed

241   together with the 6-311+G(2d,p) triple zeta basis set, which is a reasonably large, flexible

242   basis set with both polarization and diffuse functions added to the atoms. We have used this

243   level of theory previously for calculations on Fe- and Mg-containing oxides, hydroxides and

244   silicates [*Rapp et al.*, 2012; *Saunders and Plane*, 2011]. The expected uncertainty in the

245   calculated reaction enthalpies is ±20 kJ mol^{-1} at this level of theory.

9

246 Since we are interested in the reactivity of HO_2 with exposed surface sites, here we consider

247 the binding of HO_2 to either the Fe or Mg end of an $FeMgSiO_4$ unit. While this is clearly an

248 approximation of the surface, it yields useful insights into the likely mechanisms that occur

249 and is useful for interpreting the experimental observations. For each molecule the

250 geometry was first optimised, and then vibrational frequencies calculated to determine the

251 zero point energy correction. The most stable form of $FeMgSiO_4$ has quintet spin multiplicity

252 [*Saunders and Plane*, 2011] because of the presence of the Fe atom. We therefore

253 considered all possible spin multiplicities of the species involved in HO_2 uptake and

254 subsequent reaction. The results for the most stable spin states are reported here (though

255 in fact the different states of the relevant molecules are near-degenerate).

256 These calculations indicate that an exposed surface Fe atom is able to catalyse the

257 destruction of HO_2 *via* the overall reaction

258 $\qquad HO_2 + HO_2 \; \rightarrow \; H_2O_2 + O_2$ (2)

259 Figure 5 illustrates the catalytic mechanism. An HO_2 first chemisorbs to the Fe atom with a

260 substantial binding energy of 225 kJ mol^{-1} (Figure 4(a) and (b)). A second HO_2 can then

261 abstract the adsorbed H atom, in a reaction that is quite exothermic

262 (ΔH^o(0 K) = -77 kJ mol^{-1}). Note that the differing role of the two HO_2 radicals effectively

263 makes the reaction first order, reconciling this mechanism with the kinetic plots shown

264 above. This reaction occurs *via* a submerged transition state (Figure 4(c)) to yield H_2O_2 and

265 an O_2 molecule bound to the Fe atom (Figure 4(d)). Finally, a third HO_2 can displace the

266 bound O_2 exothermically (ΔH^o(0 K) = -64 kJ mol^{-1}) to yield the structure in Figure 4(b), hence

267 starting the Eley-Rideal cycle over again.

268 In contrast, when HO_2 adsorbs onto an exposed Mg, the H atom migrates onto an O of the

269 silicate group and the remaining O_2 is strongly bound to the Mg (Figure 4(e)). This process is

270 even more exothermic than adsorption to the Fe, with ΔH^o(0 K) = -342 kJ mol^{-1}. However,

271 the H atom cannot be abstracted *via* a gas-phase HO_2, because this is highly endothermic

272 (ΔH^o(0 K) = 106 kJ mol^{-1}), and the O_2 is too strongly bound to the Mg atom to be displaced.

273 Thus the adsorption effectively deactivates the Mg site.

274   These calculations therefore provide an explanation for two experimental observations: the

275   much larger value of γ for fayalite compared with forsterite; and the fact that the uptake

276   rate on olivine and fayalite reach a steady state at large contact times.

277   ***Atmospheric modelling***

278   In order to explore the impact of HO_2 uptake on MSPs, we have used WACCM (extending

279   vertically from the surface to 140 km) coupled with the CARMA aerosol microphysics model

280   [*Marsh et al.*, 2013]. This combination has previously been used by *Bardeen et al.* [2008] to

281   treat MSPs in the atmosphere and by *Frankland et al.* [2015] to examine the effect of uptake

282   to MSPs on the HNO_3 budget. A cosmic dust input rate into the atmosphere of 44 tons day^{-1}

283   is used, and this all assumed to ablate and subsequently form MSPs. Model simulations for

284   the years 2004 – 2010 were carried out with specified dynamics using a meteorological data

285   set from Goddard Earth Observing System model (GEOS) 5 below 50 km. Dynamics were

286   specified as in *Feng et al.* [2013], so that 1% of the meteorological conditions (temperature,

287   winds, surface pressure, specific humidity, surface wind stress, latent, sensible heat flux,

288   etc.) were combined with the WACCM fields below 50 km at every model dynamics time

289   step. This nudging factor then reduced linearly from 1 to 0 % between 50-60 km. Above 60

290   km there is no nudging to the re-analysis fields and the model in this region is free-running.

291   Two WACCM-CARMA simulations were run: a control experiment with no uptake of HO_2 to

292   MSPs, and a second experiment where removal was added using $\gamma = 0.2$. Comparison of the

293   2 runs then allows assessment of the importance of this process.

294   This study aims to demonstrate an impact of MSP on the atmospheric availability of HO_2 in

295   terms of when and where an impact would be observable. Quantification of such an impact

296   is not an aim since uncertainties in the uptake coefficient are both too large and too

297   complex [*Frankland et al.*, 2015]. The available surface area of MSP is also uncertain, both in

298   terms of the total mass influx and the fractal agglomerate nature of the atmospheric

299   particles [*Plane*, 2012; *Saunders et al.*, 2007].

300   An uptake coefficient (see equation E5, below) for the atmospheric modelling was chosen as

301   follows. Recent measurements have shown that HO_2 uptake tends to be more rapid for

302   higher RH (See Figure 3 in *Lakey et al.* [2015] and Figure 6 in *Matthews et al.* [2014]). This is

303   either due to dissolution of TMI (although note that as droplet size increases the

11

304   concentration of TMI decreases so that the uptake would begin to reduce again in large

305   droplets) or a $HO_2.H_2O$ complex may form on the surface and react more rapidly than HO_2

306   radicals in a similar mechanism to that proposed for the gas phase [*Stone and Rowley*,

307   2005]. Although the middle atmosphere is relatively dry, significant RH can be reached at

308   low temperatures. This occurs both in the summer mesosphere, where RH exceeds 100 %

309   and polar mesospheric ice clouds can form [*Murray and Jensen*, 2010], and in the winter

310   stratosphere where RH can reach 20 %. This is demonstrated below in Figure 7 (b), where

311   the RH from the WACCM control run is shown zonally averaged at 80° S as a function of

312   pressure and time. For the most part, however, the middle atmosphere is significantly dryer

313   than it is possible to measure using the current apparatus since H_2O is required to produce

314   HO_2. Nevertheless, as the ambient conditions move toward low RH a kinetic steady state will

315   be reached where a mechanism not involving H_2O will dominate. This will cause the uptake

316   coefficient to stabilise, as seen for example in measurements on humic acid (Figure 3 in

317   *Lakey et al.* [2015]). The uptake coefficient of ~0.07 measured here on olivine and fayalite

318   likely holds for lower RH at room temperature. At colder atmospheric temperatures this is

319   likely to increase [*Mao et al.*, 2010]. Measuring γ at other atmospheric temperatures was

320   not possible with the apparatus used in this study, however it has been noted that γ usually

321   increases with decreasing temperature [*Hayward et al.*, 1967].

322   γ =0.2 has therefore been used in the WACCM-CARMA model. This is a physically reasonable

323   value (γ as high as 0.8 have been measured in the past for HO_2 uptake on aqueous aerosol

324   [*Thornton and Abbatt*, 2005]). Such high values have previously been measured on solid

325   aerosols only when significant Cu is present, however Fe and other transition metals are

326   also known to take up HO_2 efficiently [*Mao et al.*, 2010].

327   There is considerable uncertainty in the total amount of cosmic dust entering the

328   atmosphere each day [*Rapp et al.*, 2012], and the fraction that ablates is a function of the

329   dust size and velocity distributions. Hence it is possible that the value of the ablated mass

330   input is higher by up to a factor of 3 [*Carrillo-Sánchez et al.*, 2015], which would result in a

331   larger modelled impact of MSP on the HO_2 abundance. Besides the uncertainty in the total

332   MSP mass *Saunders et al.* [2007] showed that MSPs likely consist of fractal chain aggregates

333   which would imply that the surface area they present for reaction would be significantly

334   higher than the spherical approximation used in the current modelling scheme. MSP were

12

335   input to WACCM-CARMA simulations as 0.2 nm radius primary particles (approximately

336   molecular dimensions) injected over a range of altitudes between 75 and 110 km, with the

337   peak injection rate at 83 km. Particles were then allowed to agglomerate collisionally and

338   the surface area calculated in each model time step.

339   The rate of uptake to an atmospheric aerosol is defined by

340     $$\frac{d[HO_2]}{dt} = -0.25 w \gamma A_d [HO_2] \qquad\qquad (E5)$$

341   where A_d (cm^2 cm^{-3}) is the volumetric surface area of aerosol available in the atmosphere.

342   Note that (E1) is the solution to an equation of a similar form to (E5) but differs in that the

343   former must account for losses, both to the flow tube walls and through gas phase self-

344   recombination, and considers a mean aerosol particle. In addition at the low pressures

345   (uptake in the model occurs at pressures below 5 hPa, see below) present in the middle

346   atmosphere the effect of diffusion can be neglected.

347   To assess the validity of this modelling approach, WACCM-CARMA output for the run with

348   no HO_2 uptake to MSPs was then compared to atmospheric observations from the

349   Microwave Limb Sounder (MLS data version 4.2x), a radiometer aboard the Aura satellite

350   [*Livesey et al.*, 2013; *Pickett et al.*, 2008; *Waters et al.*, 2006]. All WACCM-CARMA data has

351   been sampled at the averaging kernels used for the MLS data. This reduced the model

352   altitude resolution in the stratosphere but allows a like with like comparison. A comparison

353   for January 2005 is shown in Figure 6. The altitude range of both data sets has been

354   displayed only to the recommended scientifically valid range of the MLS data

355   (22 - 0.046 hPa, ~30 - 60 km). This is also a reasonable restriction to the WACCM-CARMA

356   data as above this altitude nudging to the specified dynamics is not applied, whilst below

357   this MSPs will be entrained in liquid sulfuric acid droplets and unable to take up HO_2. The

358   comparison in general is satisfactory: the HO_2 mixing ratio increases with altitude and is

359   fairly uniform across mid latitudes. The reduction and increase in the winter and summer

360   polar regions, respectively, are well reproduced by the model.

361   WACCM-CARMA does appear to under predict the mixing ratio at the higher altitudes

362   (around 0.05 hPa) and over predict at lower altitudes (around 5 hPa). A similar under

363   estimation at high altitude was observed by *Millán et al.* [2015], who made an extensive

364   comparison of WACCM to an offline retrieval of MLS HO_2 mixing ratio which was able to

13

365   cover a larger range of altitudes than the data used here. The authors in that study

366   speculated that either our understanding of mesospheric chemistry is incomplete, or that

367   parameterisations of solar flux may be inaccurate. *Millán et al.* [2015] did not observe the

368   over estimation at lower altitudes shown here, however this may not be present in the

369   more advanced offline HO_2 retrieval used in that study. A more thorough discussion of such

370   model discrepancies is beyond the scope of this study. Since the model broadly reproduces

371   the observations, it is deemed a useful tool for assessing the impact of heterogeneous

372   chemistry on the HO_2 abundance.

373   Figure 7 (a) illustrates the percentage difference in HO_2 volume mixing ratio, zonally

374   averaged at 80° S and plotted against time and altitude, between the WACCM run with HO_2

375   uptake and the control run. For comparison, the % RH and MSP surface area, both from the

376   control run, are shown for the same region in Figure 7 (b & c, respectively). This

377   demonstrates a clear impact on the HO_2 profile. As stated above, because of the

378   uncertainties in both the uptake coefficient (due to temperature and RH) and surface area

379   (due to the mass input and fractal nature of particles) the aim of this study is not to quantify

380   such an impact but rather to demonstrate that it is potentially significant and where and

381   when it would most likely be observed. The latitude variation of that impact is shown for

382   June 2009 in Figure 8. The strong impact (>40% removal) near the pole falls off rapidly

383   toward mid latitudes, with less than 10% removal at all altitudes by 65° S. This trend is

384   qualitatively reasonable even in light of uncertainty in the uptake coefficient, since it reflects

385   the downward transport of MSPs in the polar vortex.

386   Detection of the heterogeneous removal of HO_2 in the satellite observations is difficult for

387   two reasons. First, although a 40% removal is significant, the effect is only present during

388   the polar night (when background concentrations are relatively low) and thus difficult to

389   identify unambiguously. Second, there is a paucity of MLS-AURA measurements at very high

390   latitudes, where the impact of MSPs is greatest. In the future, improved datasets e.g. *Millán*

391   *et al.* [2015] may facilitate a more quantitative study. Nevertheless, the clear potential for

392   MSPs to influence the atmospheric HO_2 profile has implications for future modelling of

393   chemistry in the middle atmosphere.

14

Conclusions

HO$_2$ uptake to MSP analogues has been studied using a combination of laboratory techniques and atmospheric modelling. A dependence on the composition of the MSP analogue was observed. This appears to be a result of mechanistic and energetic differences between the binding of HO$_2$ to Fe and Mg sites. Uptake coefficients, γ, of $(4.3 \pm 0.4) \times 10^{-3}$, $(6.9 \pm 1.2) \times 10^{-2}$ and $(7.3 \pm 0.4) \times 10^{-2}$ were measured on forsterite, olivine and fayalite, respectively, all at RH of ~10 %.

A value for the uptake coefficient of 0.2, based on the laboratory measurements and taking into account the likely temperature and RH dependencies of γ, was applied along with a total meteoric input of 44 tons day^{-1} in WACCM-CARMA. Comparison to a control run showed that there was a significant impact on the HO$_2$ budget in the polar vortex, with reductions in the HO$_2$ volume mixing ratio of up to 40%. This impact was found to be strongly dependant on latitude, in agreement with the presence of MSPs in the polar night.

The result of the global modelling presented here should not be considered quantitatively since uncertainties in the uptake coefficient and available surface area of MSP have necessitated a rather simplistic approach. The potential for the meteoric input to be higher and the neglect of any temperature dependence of the uptake imply that this could be a lower limit to the impact of this process in the atmosphere, however the further complications of composition and humidity dependence could offset this. Future re-analysis of MLS-aura HO$_2$ measurements may facilitate a more quantitative comparison by extending the latitude range covered.

15

424 The GEOS5 meteorological analyses are available at

425 https://www.earthsystemgrid.org/home.html. The WACCM data sets are archived on a

426 University of Leeds networked server for Plane's group and available upon request to JMCP

427 or WF. The experimental data is available upon request to DEH.

428

429 **References**

430 Bardeen, C. G., O. B. Toon, E. J. Jensen, D. R. Marsh, and V. L. Harvey (2008), Numerical
431 simulations of the three-dimensional distribution of meteoric dust in the mesosphere and
432 upper stratosphere, *J. Geophys. Res.*, *113*, art. no. D17202

433 Broadley, S. L., B. J. Murray, R. J. Herbert, J. D. Atkinson, S. Dobbie, T. L. Malkin, E. Condliffe,
434 and L. Neve (2012), Immersion mode heterogeneous ice nucleation by an illite rich powder
435 representative of atmospheric mineral dust, *Atmos. Chem. Phys.*, *12*(1), 287-307

436 Brown, R. L. (1978), Tubular flow reactors with 1st-order kinetics, *J. Res. Nat. Bur. Stand.*,
437 *83*(1), 1-8

438 Carrillo-Sánchez, J. D., J. M. C. Plane, W. Feng, D. Nesvorný, and D. Janches (2015), On the
439 size and velocity distribution of cosmic dust particles entering the atmosphere, *Geophys.*
440 *Res. Lett.*, *42*(15), 6518-6525

441 Feng, W., D. R. Marsh, M. P. Chipperfield, D. Janches, J. Höffner, F. Yi, and J. M. C. Plane
442 (2013), A global atmospheric model of meteoric iron, *J. Geophys. Res.*, *118*(16), 9456-9474

443 Frankland, V. L., A. D. James, W. Feng, and J. M. C. Plane (2015), The uptake of HNO_3 on
444 meteoric smoke analogues, *J. Atmos. Sol. Terr. Phys.*, *127*, 150-160

445 Frisch, M. J. E. A., G. W. Trucks, H. B. Schlegel, G. E. Scuseria, M. A. Robb, J. R. Cheeseman, G.
446 Scalmani, V. Barone, B. Mennucci, and G. A. Petersson (2009), Gaussian 09, Revision A. 01,
447 Gaussian, *Inc., Wallingford, CT*, *200*

448 George, I. J., P. S. J. Matthews, L. K. Whalley, B. Brooks, A. Goddard, M. T. Baeza-Romero,
449 and D. E. Heard (2013), Measurements of uptake coefficients for heterogeneous loss of HO_2
450 onto submicron inorganic salt aerosols, *Phys. Chem. Chem. Phys.*, *15*(31), 12829-12845

451 Hayward, D. O., D. A. King, and F. C. Tompkins (1967), Variation of sticking probabilities with
452 temperature and coverage, and desorption spectra for nitrogen on tungsten films, *Proc.*
453 *Roy. Soc. Lond. A 297*(1450), 321-335

454 Hunten, D. M., R. P. Turco, and O. B. Toon (1980), Smoke and dust particles of meteoric
455 origin in the mesosphere and stratosphere, *J. Atmos. Sci.*, *37*(6), 1342-1357

456 Lakey, P. S. J., I. J. George, L. K. Whalley, M. T. Baeza-Romero, and D. E. Heard (2015),
457 Measurements of the HO_2 uptake coefficients onto single component organic aerosols, *Env.l*
458 *Sci. Tech.*, *49*(8), 4878-4885

459 Livesey, N. J., et al. (2013), Earth Observing System (EOS) Aura Microwave Limb Sounder
460 (MLS) version 4.2 level 2 data quality and description document,, edited by JPL, Jet
461 Propulsion Laboratory, California Institute of Technology, Pasadena, California, USA,

16

462 Mao, J., S. Fan, D. J. Jacob, and K. R. Travis (2013), Radical loss in the atmosphere from Cu-Fe
463 redox coupling in aerosols, *Atmos. Chem. Phys.*, *13*(2), 509-519

464 Mao, J., et al. (2010), Chemistry of hydrogen oxide radicals (HO_x) in the Arctic troposphere in
465 spring, *Atmos. Chem. Phys.*, *10*(13), 5823-5838

466 Marsh, D. R., M. J. Mills, D. E. Kinnison, J.-F. Lamarque, N. Calvo, and L. M. Polvani (2013),
467 Climate change from 1850 to 2005 simulated in CESM1(WACCM), *J. Climate*, *26*(19), 7372-
468 7391

469 Matthews, P. S. J., M. T. Baeza-Romero, L. K. Whalley, and D. E. Heard (2014), Uptake of HO_2
470 radicals onto Arizona test dust particles using an aerosol flow tube, *Atmos. Chem. Phys.*,
471 *14*(14), 7397-7408

472 Millán, L., S. Wang, N. Livesey, D. Kinnison, H. Sagawa, and Y. Kasai (2015), Stratospheric and
473 mesospheric HO_2 observations from the Aura Microwave Limb Sounder, *Atmos. Chem.*
474 *Phys.*, *15*(5), 2889-2902

475 Mozurkewich, M., P. H. McMurry, A. Gupta, and J. G. Calvert (1987), Mass accommodation
476 coefficient for HO_2 radicals on aqueous particles, *J. Geophys. Res.*, *92*(D4), 4163-4170

477 Murray, B. J., and E. J. Jensen (2010), Homogeneous nucleation of amorphous solid water
478 particles in the upper mesosphere, *J. Atmos. and Sol. Terr. Phys.*, *72*(1), 51-61

479 Murray, B. J., and J. M. C. Plane (2005), Modelling the impact of noctilucent cloud formation
480 on atomic oxygen and other minor constituents of the summer mesosphere, *Atmos. Chem.*
481 *Phys.*, *5*(4), 1027-1038

482 Pickett, H. M., B. J. Drouin, T. Canty, R. J. Salawitch, R. A. Fuller, V. S. Perun, N. J. Livesey, J.
483 W. Waters, R. A. Stachnik, and S. P. Sander (2008), Validation of aura microwave limb
484 sounder OH and HO_2 measurements, *J. Geophys. Res.*, *113*, art. no. D16S30

485 Plane, J. M. C. (2012), Cosmic dust in the Earth's atmosphere, *Chem. Soc. Rev.*, *41*(19), 6507-
486 6518

487 Plane, J. M. C., W. Feng, and E. C. M. Dawkins (2015), The mesosphere and metals:
488 Chemistry and changes, *Chem. Rev.*, *115*(10), 4497-4541

489 Rapp, M., J. M. C. Plane, B. Strelnikov, G. Stober, S. Ernst, J. Hedin, M. Friedrich, and U. P.
490 Hoppe (2012), In situ observations of meteor smoke particles (MSP) during the Geminids
491 2010: constraints on MSP size, work function and composition, *Ann. Geophys.*, *30*(12), 1661

492 Saunders, R. W., S. Dhomse, W. S. Tian, M. P. Chipperfield, and J. M. C. Plane (2012),
493 Interactions of meteoric smoke particles with sulphuric acid in the Earth's stratosphere,
494 *Atmos. Chem. Phys.*, *12*(10), 4387-4398

495 Saunders, R. W., P. M. Forster, and J. M. C. Plane (2007), Potential climatic effects of
496 meteoric smoke in the Earth's paleo-atmosphere, *Geophys. Res. Lett.*, *34*, art. no. L16801

497 Saunders, R. W., and J. M. C. Plane (2006), A laboratory study of meteor smoke analogues:
498 composition, optical properties and growth kinetics, *J. Atmos. and Sol. Terr. Phys.*, *68*(18),
499 2182-2202

500 Saunders, R. W., and J. M. C. Plane (2011), A photo-chemical method for the production of
501 olivine nanoparticles as cosmic dust analogues, *Icarus*, *212*(1), 373-382

17

502 Siskind, D. E., M. H. Stevens, C. R. Englert, and M. G. Mlynczak (2013), Comparison of a
503 photochemical model with observations of mesospheric hydroxyl and ozone, *J. Geophys.*
504 *Res.*, *118*(1), 195-207

505 Stone, D., and D. M. Rowley (2005), Kinetics of the gas phase HO_2 self-reaction: Effects of
506 temperature, pressure, water and methanol vapours, *Phys.Chem. Chem. Phys.*, *7*(10), 2156-
507 2163

508 Stone, D., L. K. Whalley, and D. E. Heard (2012), Tropospheric OH and HO_2 radicals: field
509 measurements and model comparisons, *Chem. Soc. Rev.*, *41*(19), 6348-6404

510 Summers, M. E., and D. E. Siskind (1999), Surface recombination of O and H_2 on meteoric
511 dust as a source of mesospheric water vapor, *Geophys. Res. Lett.*, *26*(13), 1837-1840

512 Thornton, J., and J. P. D. Abbatt (2005), Measurements of HO_2 uptake to aqueous aerosol:
513 Mass accommodation coefficients and net reactive loss, *J. Geophys. Res.*, *110*, art. no.
514 D08309

515 Waters, J. W., et al. (2006), The Earth observing system microwave limb sounder (EOS MLS)
516 on the aura Satellite, *IEEE Trans. Geosci. Remote Sensing*, *44*(5), 1075-1092

517

518 **Table Headings**

519 **Table 1** Values of γ measured in this study.

520 **Tables**

521 **Table 1** Values of γ measured in this study.

522

MSP analogue	RH / %	Measured γ	R^2 (see Fig. 4 a)
Forsterite	11.6	$(4.3 \pm 0.4) \times 10^{-3}$	0.953
Olivine	10.0	$(6.9 \pm 1.2) \times 10^{-2}$	0.985
Fayalite	9.9	$(7.3 \pm 0.4) \times 10^{-2}$	0.945

523

524

525 **Figure Captions**

526 **Figure 1** Schematic diagram of the experimental system. Abbreviated components:

527 Condensation Particle Counter (CPC), Mass Flow Controller (MFC) and Photo-Multiplier Tube

528 (PMT).

18

529 **Figure 2** Measured size distribution of fayalite at 9.9 % RH, normalised to the peak of a log

530 normal fit to the distribution. Ten individual measurements are shown in grey with the

531 mean in black and a log normal fit (mean and standard deviation of 368 nm and 0.680

532 respectively) to the size distribution in red.

533 **Figure 3** (a) Example plot showing the anti-correlation of HO_2 signal to number

534 concentration of fayalite MSP analogue particles (at 9.9 % RH with a residence time of

535 20.6 s). (b) Example plot showing the HO_2 signal variation with fayalite aerosol number

536 concentration, also at 9.9 % RH for three fixed contact times as shown in the legend. Full

537 experimental conditions are given in the text. Means and standard deviations of three

538 condensation particle counter and FAGE measurements are shown (as points and error bars,

539 respectively).

540 **Figure 4** (a) Plot of the dimensionless quantity $0.25\gamma_{obs}wA_dt$ as a function of reaction time for

541 uptake of HO_2 onto fayalite at a RH = 9.9%. The linear least-squares fit to these point yields

542 $0.25\gamma_{obs}wA_d$ as the gradient, $(6.3 \pm 1.4) \times 10^{-6}$ in this case, from which $\gamma_{obs} = (7.3 \pm 0.4) \times 10^{-2}$

543 was obtained. The intercept of the fit at $t = 0$ $((2.3 \pm 1.8) \times 10^{-5})$ suggests a higher gradient

544 and hence a higher uptake coefficient occurring in the first few seconds of contact between

545 the HO_2 and fayalite aerosols. The error bars represent 2 standard deviations in the

546 individual exponential fits, examples of which are given in Figure 3(b). (b) Plot of γ_{obs}

547 determined from a straight line from the origin to each point in panel (a), demonstrating

548 that over time γ_{obs} decreases toward the value obtained from the straight line fit shown in

549 panel (a).

550 **Figure 5** Electronic structure calculations at the B3LYP/6-311+g(2d,p) level of theory with

551 enthalpies in kJ mol^{-1} in brackets: (a) HO_2 uptake on an exposed Fe atom on the olivine

552 surface leads to a chemisorbed adduct (b); a second HO_2 can now abstract the adsorbed H

553 atom via transition state (c) to form (d), where O_2 is bound to the Fe atom, which can then

554 be displaced by a further HO_2 to yield (b). When HO_2 adds to an exposed Mg atom,

555 chemisorption leads to the very stable structure (e).

556 **Figure 6** (a) Zonal average HO_2 mixing ratio (ppbv) as measured by the Microwave Limb

557 Sounder (MLS) for January 2005. (b) Zonal average HO_2 mixing ratio (ppbv) as predicted by

558 WACCM-CARMA simulations using specified dynamics for January 2005, from a control

559 simulation with no heterogeneous uptake of HO_2. The colour bar applies to both panels but

19

560   should be interpreted with caution since a nonlinear colour scaling has been used to display

561   the full range of the data.

562   **Figure 7** (a) Percentage difference in HO_2 volume mixing ratio between a WACCM-CARMA

563   simulation with γ = 0.2 and a 'control' simulation with γ = 0. (b) % RH in the control

564   simulation. (c) Available surface area (μm^2 cm^{-3}) of MSP from the WACCM-CARMA control

565   simulation. Data for all panels is zonally averaged at 80° S. Colour bars are included to aid

566   the reader, however these should be treated with caution since nonlinear colour scaling has

567   been used to accentuate features in each panel.

568   **Figure 8** Percentage difference in HO_2 volume mixing ratio between the two model runs as a

569   function of latitude for June 2009. The colour bar should be interpreted with caution as

570   nonlinear colour scaling has been used to accentuate features in the plot.

571

20

Figure 1.

Neutralizer

Aerosol flow

Impactor

N₂

Stir bar

Dust sample

Stirrer plate

Filter

Humidified flow

MFC

MFC

N₂

Bubblers

MFC

MFC

Conditioning
flow tube

Mercury lamp

PMT

FAGE
Cell

To pump

Reaction flow tube

Injector

NO

MFC

RH/
T

CPC

Figure 2.

Figure 3.

(a)

HO₂ Signal / arb. — HO₂ Signal, Aerosol number density

(b)

ln(HO₂ Signal) / arb. vs Particle Number Density / particles cm⁻³

8.8 s, 14.7 s, 20.6 s

Figure 4.

Figure 5.

(a) Particle

+ HO$_2$ (-225)

(b)

+ HO$_2$ (-12)

(c)

- H$_2$O$_2$ (-65)

+ HO$_2$
- O$_2$ (-64)

(d)

2Å

(e)
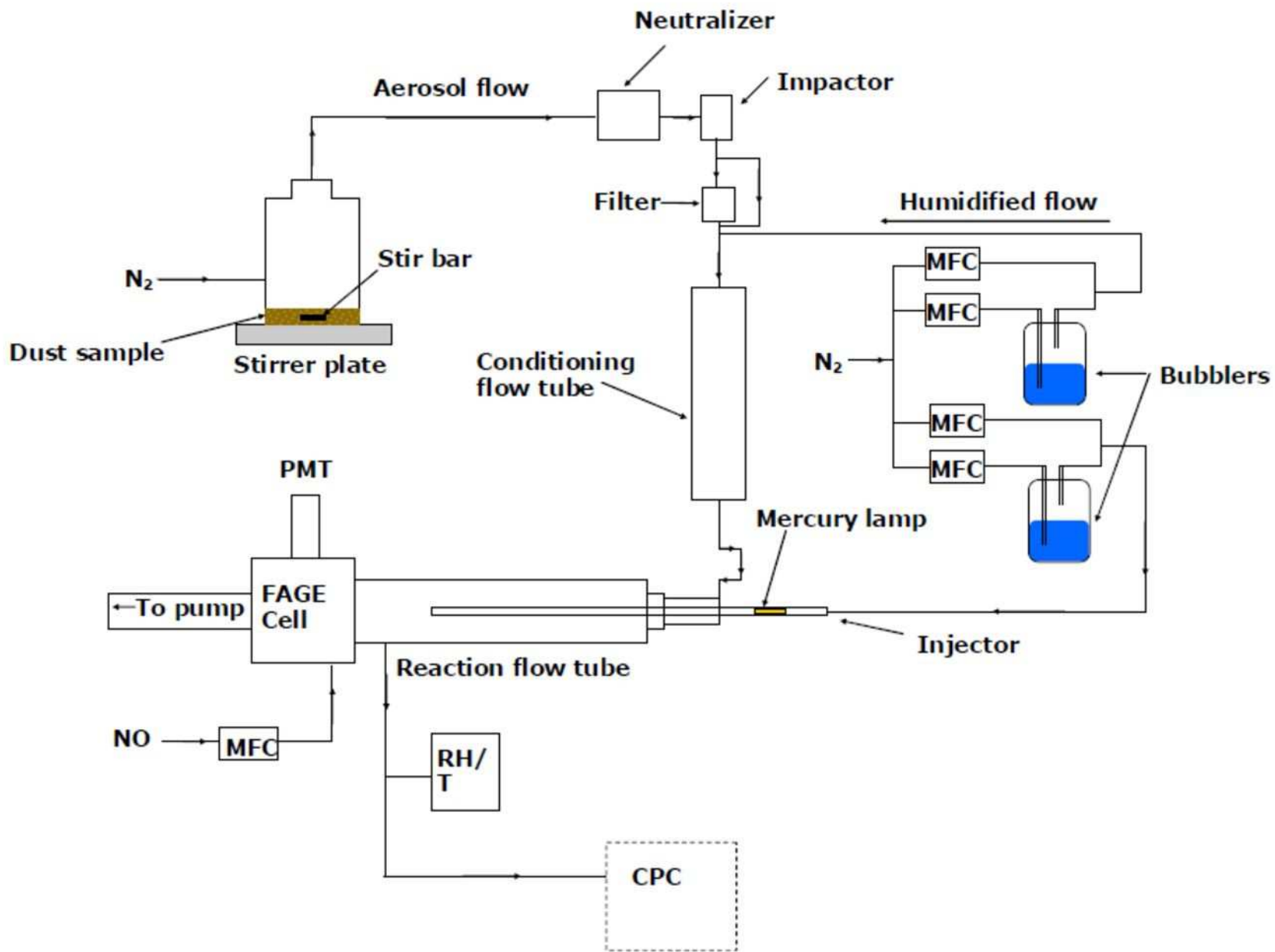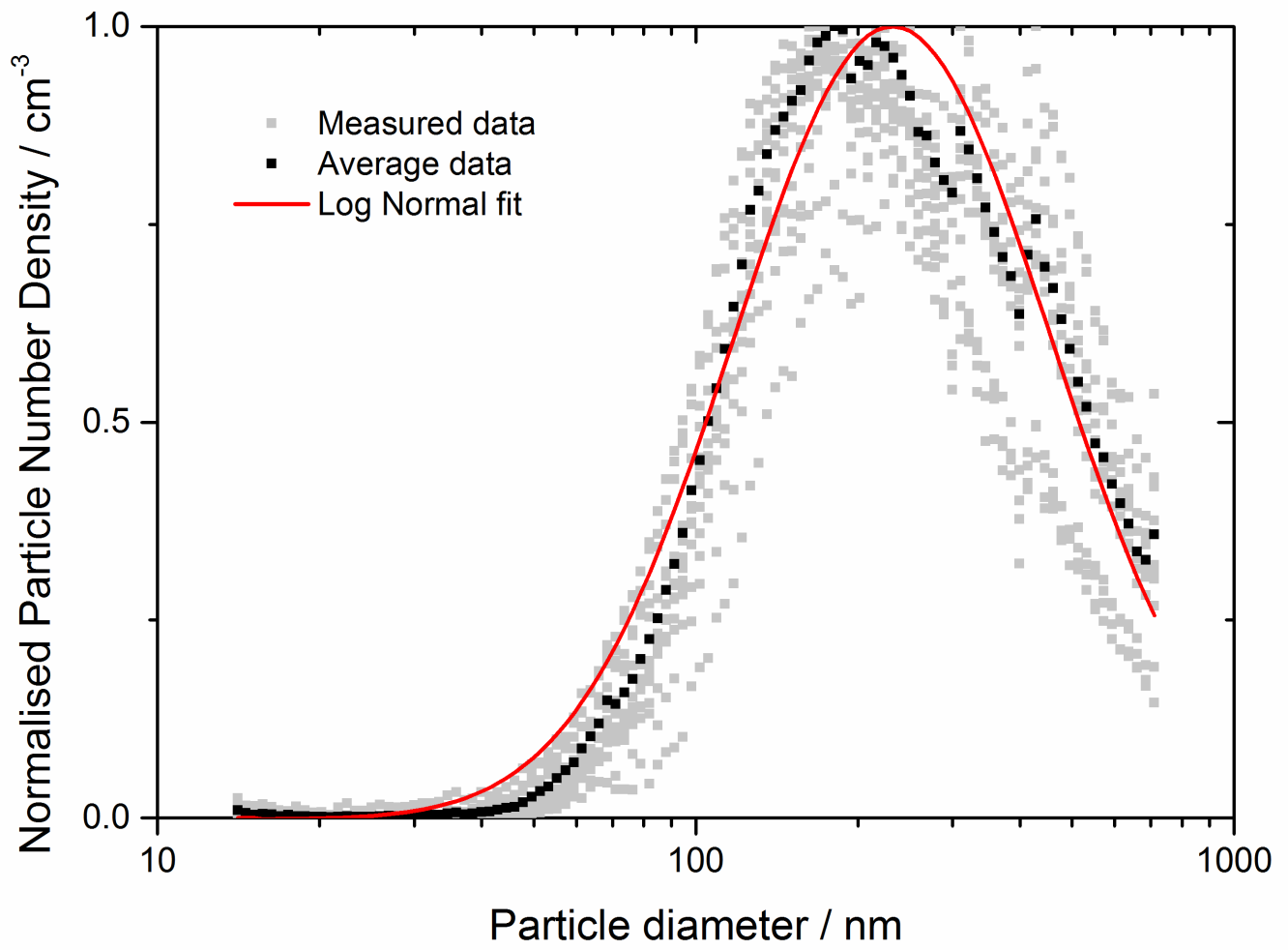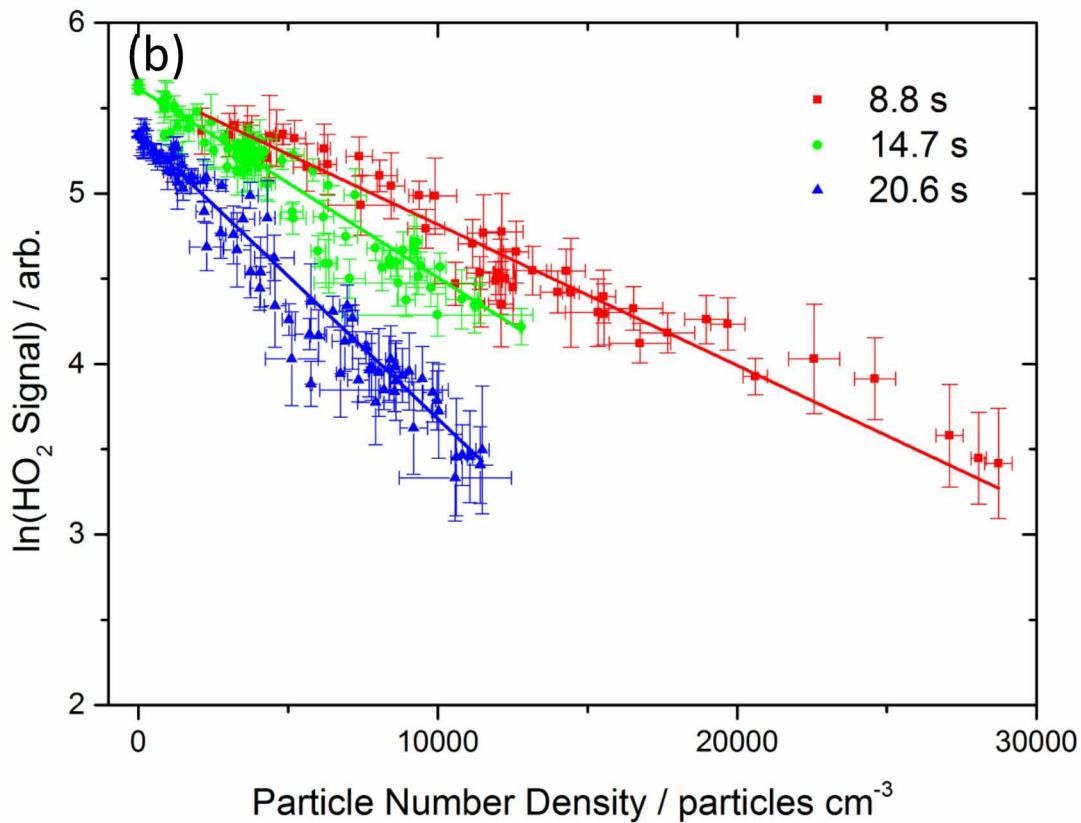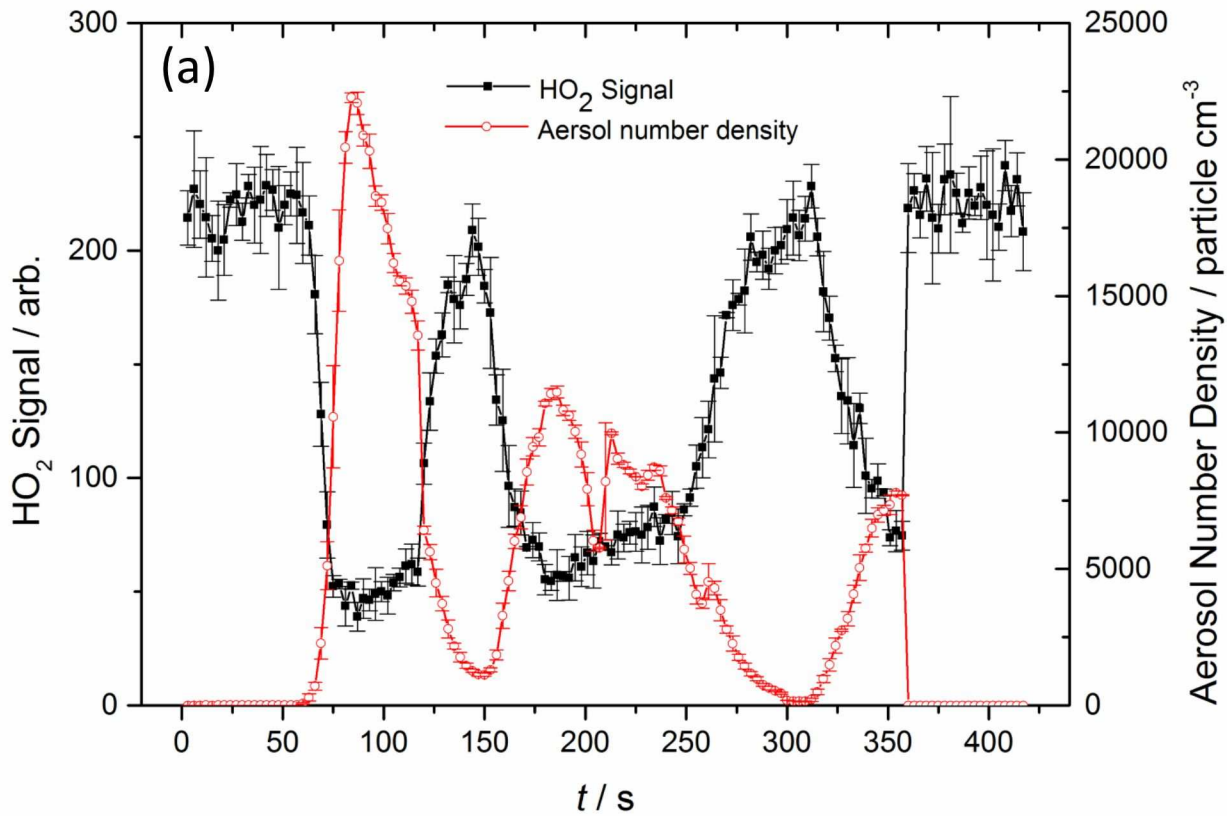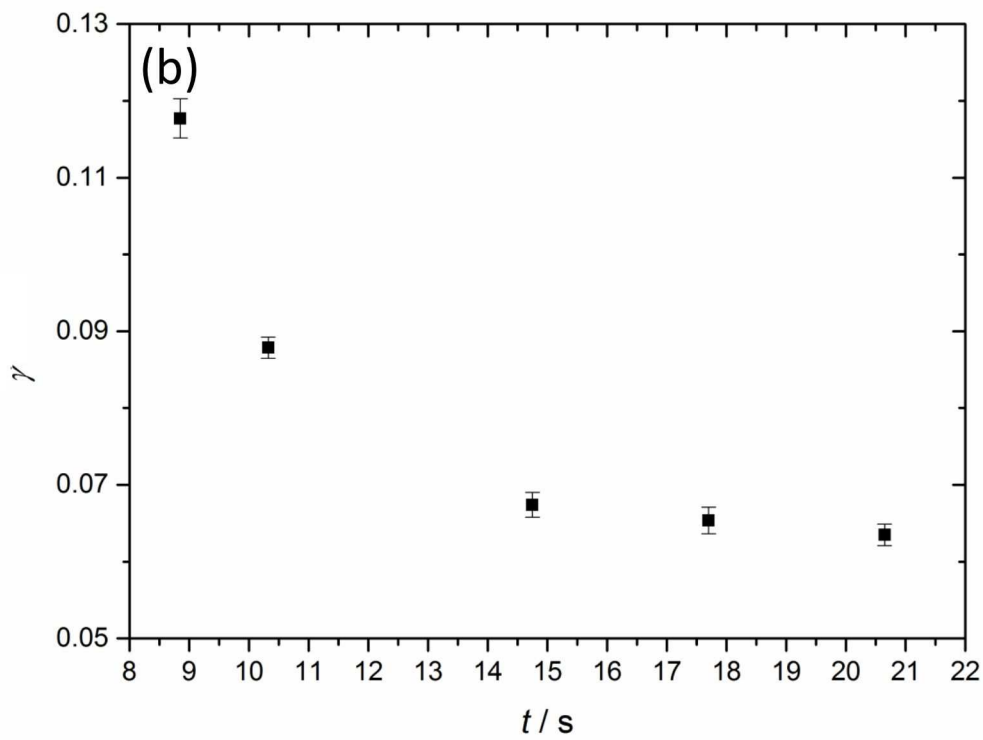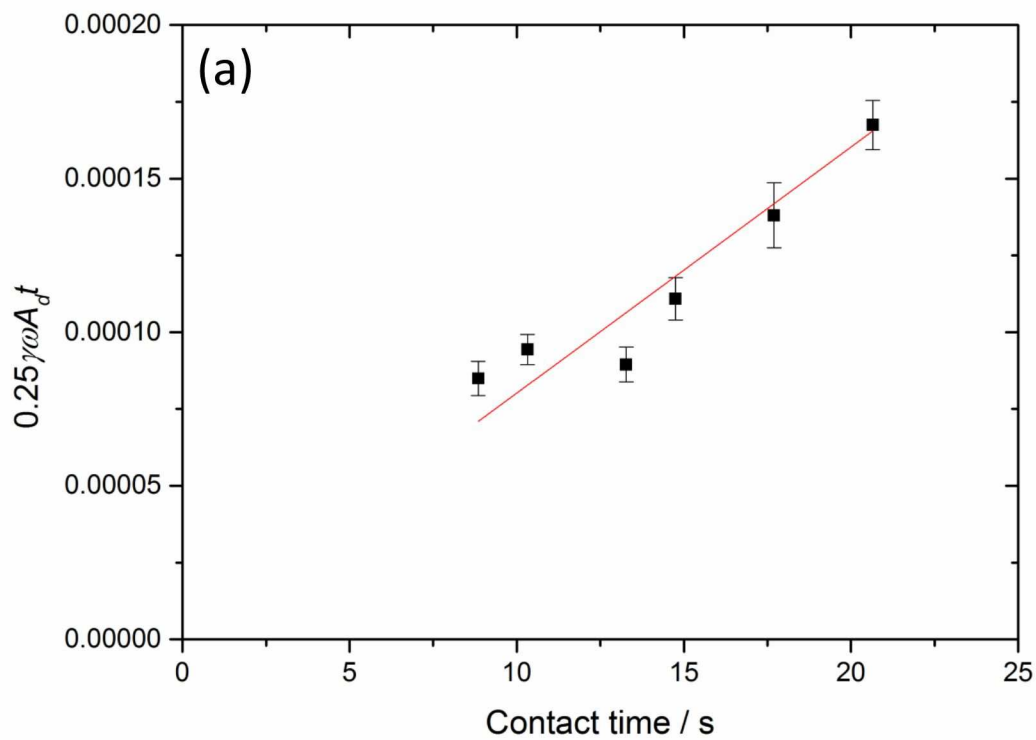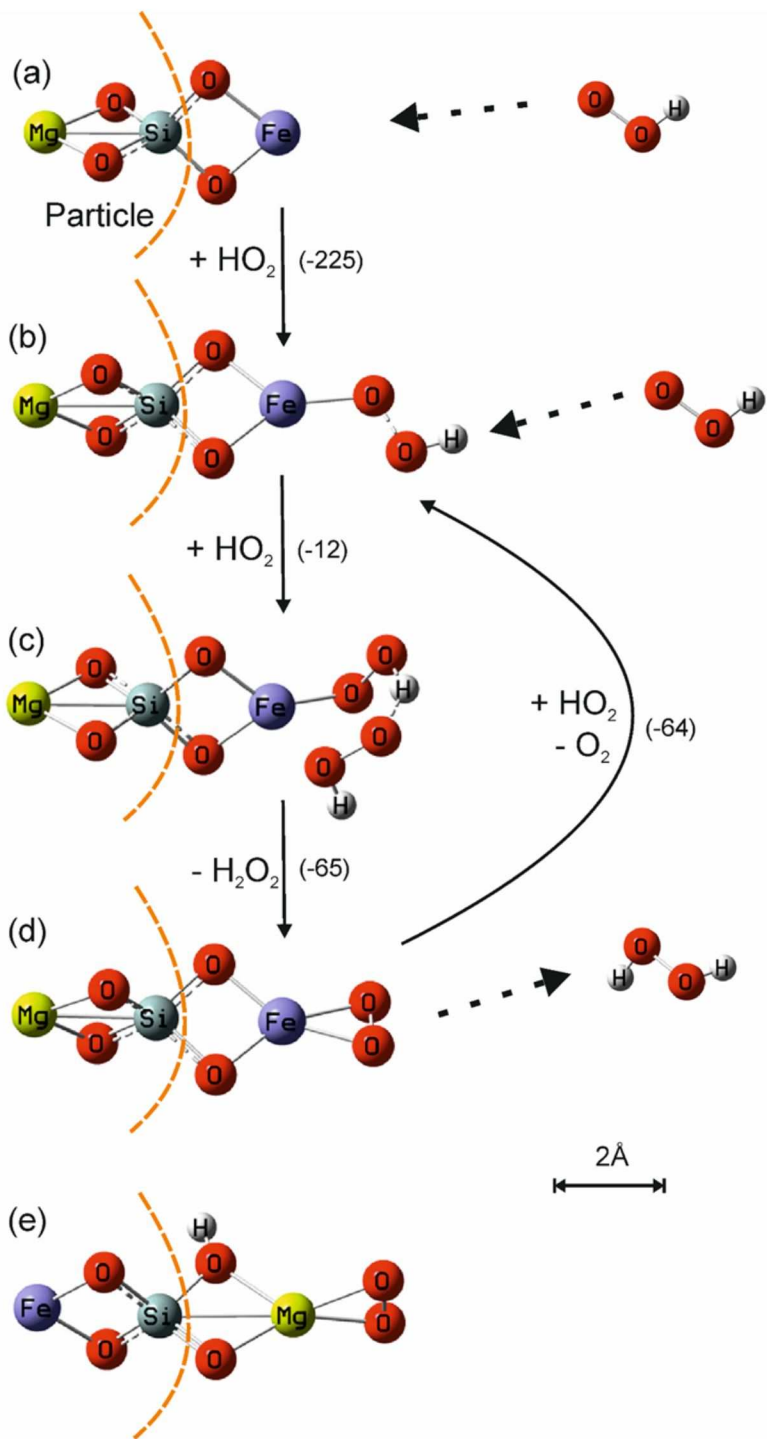
Figure 6.

Figure 7.

Figure 8.